Title: Enhancing Temperature Stability in Potassium-Sodium Niobate Ceramics through Phase Boundary and Composition Design

Authors: Xiang Lv, Jiagang Wu, Chunlin Zhao, Dingquan Xiao, Jianguo Zhu, Zehui Zhang, Chenhui Zhang, Xi-xiang Zhang

PII: S0955-2219(18)30535-1
DOI: https://doi.org/10.1016/j.jeurceramsoc.2018.08.039
Reference: JECS 12064

To appear in: *Journal of the European Ceramic Society*

Received date: 2-3-2018
Revised date: 23-8-2018
Accepted date: 24-8-2018

Please cite this article as: Lv X, Wu J, Zhao C, Xiao D, Zhu J, Zhang Z, Zhang C, Zhang X-xiang, Enhancing Temperature Stability in Potassium-Sodium Niobate Ceramics through Phase Boundary and Composition Design, *Journal of the European Ceramic Society* (2018), https://doi.org/10.1016/j.jeurceramsoc.2018.08.039

Enhancing Temperature Stability in Potassium-Sodium Niobate Ceramics through Phase Boundary and Composition Design

Xiang Lv[a,b], Jiagang Wu[a*], Chunlin Zhao[a], Dingquan Xiao[a], Jianguo Zhu[a], Zehui Zhang[b], Chenhui Zhang[b], and Xi-xiang Zhang[b*]

[a]*Department of Materials Science, Sichuan University, Chengdu 610064, P. R. China*

[b]*King Abdullah University of Science and Technology (KAUST), Physical Science and Engineering Division (PSE), Thuwal 23955-6900, Saudi Arabia*

[a*]Correspondence e-mail: wujiagang0208@163.com and msewujg@scu.edu.cn
[b*]Correspondence e-mail: xixiang.zhang@kaust.edu.sa

Abstract: Phase boundaries and composition design were explored to achieve both high piezoelectricity and favorable temperature stability in potassium-sodium niobate ceramics, using (1-*x*)(K,Na)(Nb,Sb)O_3-*x*Bi(Na,K)(Zr,Sn,Hf)O_3 ceramics. A rhombohedral-tetragonal (R-T) phase boundary was constructed at *x*=0.035-0.04 by co-doping with Sb^{5+} and Bi(Na,K)(Zr,Sn,Hf)O_3. More importantly, a superior temperature stability was observed in the ceramics with *x*=0.035, accompanying with a stable unipolar strain at room temperature to 100 °C. The ceramics with *x*=0.035 also exhibited improved piezoelectric properties (e.g., piezoelectric coefficient d_{33}~465 pC/N and electromechanical coupling factor k_p=0.47) and Curie temperature (T_c~240 °C). The Rietveld refinement and *in-situ* temperature-dependent piezoresponse force microscopy (PFM) results indicated that the enhancement of the

piezoelectric properties was caused by the easy domain switching, high tetragonal fraction, and tetragonality, while the improved temperature stability mainly originated from the stable domain structures.

abbreviation: I_{002}) was obviously higher (two times stronger) than that of $(200)_{pc}$ (abbreviation: I_{200}), suggesting the existence of an orthorhombic (O) phase [24]. As x increased, the intensities of these two peaks varied oppositely, i.e., I_{002} decreased when I_{200} increased, suggesting that the tetragonal (T) phase gradually dominated [25]. In the ceramics with x=0.05, a ratio of 2:1 between I_{200} and I_{002} was observed, indicating a dominant T phase. Fig. 2(c) shows the enlarge XRD patterns of 0.965KNNS-0.035BNKM (M=Zr, Hf, and Sn) ceramics. 0.965KNNS-0.035BNKM (M=Zr and Hf) ceramics exhibited a phase structure similar to that of 0.965KNNS-0.035BNKZSH ceramics, while 0.965KNNS-0.035BNKS ceramics showed a single peak in the 2θ range of 44-47°, indicating the existence of a pseudocubic phase [26]. Hence, it is necessary to further analyze the phase structure of each component, for example the permittivity against temperature (ε_r-T) curves.

Keywords: Lead-free ceramics; Temperature stability; KNN; R-T phase boundary

1. Introduction

Potassium-sodium niobate (KNN)-based lead-free ceramics have been extensively investigated in last two decades as one of the most promising candidates to replace the environmentally harmful lead-based piezoelectric materials in electronic devices [1-3]. However, lead-based piezoelectric ceramics still outperform those based on KNN in terms of piezoelectricity and temperature stability, the key parameters determining the overall performance of a piezoelectric material [1-3]. Studies show that it is

difficult to achieve high piezoelectricity and temperature stability simultaneously in KNN-based ceramics [4]. Different strategies, such as engineering phase boundaries, new sintering methods, etc., have been employed to meet the requirements of practical applications [4].

Among these strategies, engineering the phase boundary is the most promising to simultaneously achieve high piezoelectricity and good temperature stability in KNN-based ceramics [4]. In 2004, Saito *et al*. reported a large d_{33} (~416 pC/N) and a high T_c (~253 ^oC) in highly textured LF4T ceramics that possessed an orthorhombic-tetragonal (O-T) phase boundary [5]. The excellent temperature stability observed in these textured LF4T ceramics was comparable to that of commercial lead-based PZT-4 ceramics [5]. Although the highly textured LF4T ceramics satisfying the practical applications were synthesized by the high cost reactive template grain growth (RTGG) method, the results ignited the researchers' passion of studying KNN-based ceramics, particularly the construction of phase boundary [4]. Among the different phase boundaries, e.g., rhombohedral-orthorhombic (R-O), O-T, and rhombohedral-tetragonal (R-T), the R-T phase boundary is the most effective for enhancing the temperature stability and piezoelectricity of KNN-based ceramics [6-8].

Recent studies have shown that, in addition to the phase boundary, composition design also significantly affects the temperature stability and piezoelectric properties of KNN-based ceramics with an R-T phase boundary [9,10]. For example, in $0.96(K,Na)(Nb,Sb)O_3$-$0.04(Bi,K)(Zr,Sn)O_3$ ceramics with an R-T phase boundary and a high d_{33} of 430 pC/N, the unipolar strain declined from 0.14% to 0.09% (variation less than 40%) as temperature increased from room temperature to 190 ^oC [9]. However, the ceramics with a different composition of $(K,Na)NbO_3$-$(Bi,Li)TiO_3$-$BaZrO_3$ and a moderate d_{33} of 348 pC/N, the unipolar strain reduced more than 45%

as temperature increased from 30 ºC to 200 ºC [10]. Therefore, the R-T phase boundary and composition design are both critical to the overall performance of KNN-based lead-free ceramics [6-10].

Experiments have demonstrated that KNN-based ceramics must be doped with additives in order to construct the R-T phase boundary at or near room temperature by elevating the R-O phase transition temperature ($T_{R\text{-}O}$) and decreasing the O-T phase transition temperature ($T_{O\text{-}T}$) [4]. For instance, the addition of Sb^{5+}, $Bi_{0.5}Na_{0.5}ZrO_3$, or $Bi_{0.5}Na_{0.5}HfO_3$ simultaneously increases the $T_{R\text{-}O}$ and reduces the $T_{O\text{-}T}$ of KNN-based ceramics [4,11-13]. Recently, the addition of Sn^{4+} was reported to greatly improve the piezoelectric properties of barium titanate ($BaTiO_3$, BT) based ceramics [14-16]. More encouragingly, the giant d_{33} values of 500-697 pC/N were achieved by substituting Ti^{4+} with Sn^{4+} in BT-based ceramics [14-16]. Experiments proved that the addition of Sn^{4+} could quickly construct the phase coexistence and increase the diffuseness of phase transition, resulting in the ultrahigh dielectric and piezoelectric properties in $Ba(Ti,Sn)O_3$ ceramics [14-16]. Moreover, it is worth noting that the increased diffuseness of phase transition could also enhance the temperature stability [17]. Motivated by the above successes, both improved piezoelectricity and favorable temperature stability are highly anticipated in KNN-based ceramics using Sn^{4+} substitution.

In this work, we developed a new additive, $Bi_{0.5}(Na_{0.5}K_{0.5})_{0.5}Zr_{0.8}Sn_{0.1}Hf_{0.1}O_3$, with the purpose of simultaneously enhancing piezoelectricity and temperature stability of KNN-based ceramics. Our design was inspired by the outstanding performance of Sn^{4+} substitution in BT-based, particularly the ultrahigh piezoelectric properties and increased diffuseness of phase transition. In addition, the similar ionic radii of Zr^{4+}, Hf^{4+}, and Sn^{4+} ions (CN=6, r_{Zr}=0.072nm, r_{Hf}=0.071nm, and r_{Sn}=0.069nm) could

guarantee the sinterability of KNN-based ceramics [18], which further manifested the reliability of designed additive. In this work, we synthesized (1-*x*)($K_{0.5}Na_{0.5}$)($Nb_{0.955}Sb_{0.045}$)O_3-*x*$Bi_{0.5}$($Na_{0.5}K_{0.5}$)$_{0.5}Zr_{0.8}Sn_{0.1}Hf_{0.1}O_3$ {(1-*x*)KNNS-*x*BNKZSH} ceramics using the conventional solid-state reaction method. Our results showed that co-doping with Sb^{5+} and BNKZSH simultaneously improved the electrical properties of the KNN-based ceramics and guaranteed good temperature stability.

2. Experimental procedure

In this work, (1-*x*)KNNS-*x*BNKZSH (*x*=0.01-0.05) ceramics were fabricated by the conventional solid-state method. For comparison, 0.965KNNS-0.035BNKM (M=Zr, Hf, and Sn) ceramics were also prepared. The raw materials were K_2CO_3 (99%), Na_2CO_3 (99.8%), Nb_2O_5 (99.5%), Bi_2O_3 (99.999%), Sb_2O_3 (99.99%), HfO_2 (99.9%), and SnO_2 (99.5%) (Sinopharm Chemical Reagent Co., Ltd, CN). Mixtures of the raw materials with the designed compositions were ball-milled for 24 h with zirconia ball media and alcohol in plastic jars. Then, the dried slurry was calcined at 850 ^oC for 6 h. The calcined powder was pressed into disks of 10 mm diameter and 1 mm thickness under 10 MPa using PVA as a binder. After burning off the PVA at 500 ^oC, the disks were sintered at 1060-1120 ^oC for 3 h under a corundum crucible in air.

The structures of the ceramics were explored using X-ray diffraction (XRD) characterization (Bruker D8 Advanced XRD, Bruker AXS Inc., Madison, WI, CuK_α). For the Rietveld refinement, a high-resolution XRD instrument, X' Pert Pro MPD (DY 120 PANalytical, Netherlands), was used to collect the XRD data from the polished and annealed samples. The Maud software package and $KNbO_3$ mode was used to perform the Rietveld refinement. The parameters that were considered for

Rietveld refinement were lattice parameters, atomic positions, crystalline sizes, structural factors and phase fraction [19]. The temperature-dependent Raman spectra were measured using a Horiba Aramis Raman spectrometer (Horiba Scientific, France) with an excitation source of 473 nm. The temperature was controlled by a Linkam cell (Linkam Scientific Instruments, UK).

To characterize the electric properties of the materials, silver paste was printed on both sides of the as-sintered disks, which were then baked at 600 ^{o}C for 30 min to form reliable electrodes. Then, the disks were poled at room temperature in a silicone oil bath by applying an electric field of 4 kV/mm for 30 min. After aging for 24 h, the d_{33} values of the poled disks were measured using a quasi-static piezo-d_{33} meter (ZJ-3 A, China), and the k_p values were measured using an impedance analyzer (HP 4299A, Palo Alto, CA). The polarization-electric field (*P*-*E*) loops and strain-electric field (*S*-*E*) curves were measured using a ferroelectric analyzer (aixACCT TF Analyzer 2000, Germany) with a laser interferometer vibrometer (SP-S120/500, sios Mebtechnik GmbH, Germany), at a frequency of 1 Hz. The room-temperature permittivity (ε_r) and loss factor (tan δ) were measured using an LCR meter (Agilent 4294, USA) at a frequency of 10 kHz. The temperature dependence of ε_r was measured using a broadband dielectric spectrometer (Novocontrol Technologies GmbH, Germany).

The as-sintered samples were broken into two pieces. The cross-section of sample was mechanically polished and then thermally etched at a temperature that is lower 100 ^{o}C than sintering temperature for 15 min. Field emission scanning electron microscopy (FE-SEM, JSM-7500F, Hitachi, Japan) was used to observe the morphologies of thermally etched cross-section and perform the energy dispersive spectroscopy (EDS) analysis. To perform the piezoresponse force microscopy (PFM), the as-sintered disks were mechanically polished to a thickness of about 20 μm. The

PFM observations were conducted on a commercial atomic force microscope (MFP-3D, Asylum Research, Goleta, CA) with a conductive Pt-Ir-coated cantilever PPP-NCHPt (Nanosensors, Switzerland). To write the domains, the selected areas were poled at a bias voltage of ±10 V to completely switch the surface domains. Both the piezoresponse and phase images were recorded by applying an AC voltage (i.e., U_{ac}=±1V and f_{ac}=50 kHz). The *in situ* temperature-dependent piezoresponse images and phase images were recorded by applying an AC voltage (i.e., U_{ac}=±1V and f_{ac}=50 kHz) at different temperatures.

The *ab initio* calculations were carried out using the CASTEP program (Dassault Systèmes BIOVIA) [20]. The generalized gradient approximation (GGA) of Perdew, Burke, and Ernzernhof (PBE) was used to determine the exchange-correlation potential. The cut-off energy was set to 660 eV and the Brillouin zone was sampled using a 6×6×6 Monkhorst-Pack grid. For each phase, the experimental lattice constant of the $(K_{0.5}Na_{0.5})NbO_3$ cell was fixed while the atomic sites were fully relaxed to a force tolerance of 0.01 eV/Å. The virtual crystal approximation (VCA) method was utilized to simulate the real atom distribution in the disordered crystals [21].

3. Results and discussion

Figs. 1(a)-(d) show the FE-SEM images of polished and thermally etched cross-sections of (1-*x*)KNNS-*x*BNKZSH ceramics. Except for the ceramics with *x*=0.05, all other compositions showed a bimodal distribution containing “large” and “small” grains, and the grain sizes of the ceramics depended strongly on the doping contents. Some pores occurred in the ceramics with *x*=0.01-0.02 [Figs. 1(a) and (b)], which were easily found in lead-free ceramics due to the different growth rates in samples

[22]. Therefore, these pores were responsible for the relatively low density [see Table S1 in Supporting Information]. As *x* increased up to 0.035, the relatively dense cross-section was observed, as shown in Fig. 1(c). Thus, the appropriate addition of BNKZSH could promote the density of KNN-based ceramics, as proved by increased relative density [see Table S1 in Supporting Information]. Furthermore, some small grains were also found to attach to the large grains [Fig. 1(c)], indicating the promoted bimodal distribution. The enlarged view of small grains can be clearly seen in Figure S1(c) [see Supporting Information]. While the ultra-fine grains were observed in the ceramics with *x*=0.05, probably owing to the excess addition of additive (i.e., BNKZSH) that gathered at the grain boundaries and hindered grain growth [23]. Fig. 1(h) shows the evolution of average grain size (AGS) of (1-*x*)KNNS-*x*BNKZSH ceramics varying with *x*. The detailed statistics of grain size distribution were shown in Figure S1 [Supporting Information]. With an increase of *x*, AGS firstly increased slightly at *x*=0.01-0.035, and then reduced sharply at *x*=0.035-0.05.

Figs. 1(e)-(g) display the FE-SEM images of polished and thermally etched cross-sections of 0.965KNNS-0.035BNKM (M=Zr, Hf, and Sn) ceramics. It was found that 0.965KNNS-0.035BNKM (M=Zr and Hf) ceramics exhibited the similar cross-section morphology with respect to that of (1-*x*)KNNS-*x*BNKZSH ceramics with *x*=0.01-0.02. Therefore, these compositions exhibited the similar AGS [Fig. 1(h)]. While 0.965KNNS-0.035BNKM (M=Zr and Hf) ceramics exhibited the slightly higher density than those of (1-*x*)KNNS-*x*BNKZSH ceramics with *x*=0.01-0.02, owing to less pores [see Table S1 in Supporting Information]. However, no clear grain boundaries could be observed in 0.965KNNS-0.035BNKS ceramics [Fig. 4(g)]. The similar phenomenon was also reported in other KNN-based ceramics with a high Sn^{4+} concentration [23]. Considering the abnormal grains in 0.965KNNS-0.035BNKS

ceramics, the EDS analysis was performed to check the element distribution [see Figures S2 and S3 in Supporting Information]. The results demonstrated that all elements exhibited a homogeneous distribution, manifesting that Sn^{4+} completely diffused into the crystal lattice of the KNN-based ceramics instead of forming other secondary phases.

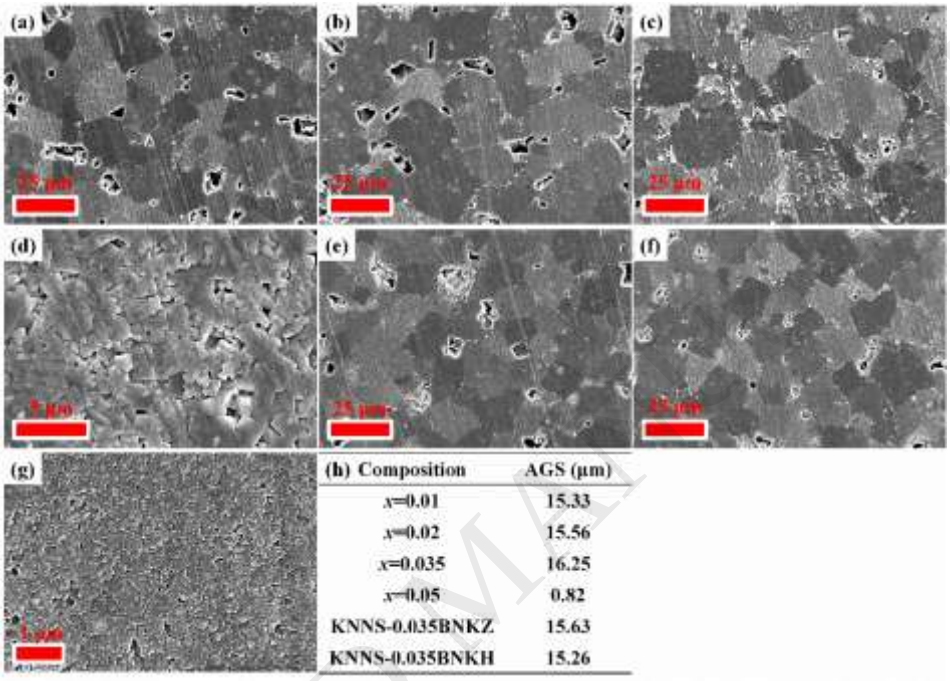

Figure 1. FE-SEM images of polished and thermally etched cross-sections of KNNS-*x*BNKZSH ceramics with (a) *x*=0.01, (b) *x*=0.02, (c) *x*=0.035, (d) *x*=0.05, and 0.965KNNS-0.035BNKM ceramics with (e) M=Zr, (f) M=Hf and (g) M=Sn. (h) Average grain size (AGS) of the ceramics in this work.

A typical and pure perovskite structure was observed in all of the samples [see Figure S1 in Supporting Information]. Figs. 2(a) and (c) display the enlarged XRD patterns for 2θ=44-46°. The phase structure of the ceramics was strongly dependent on the additive content. For (1-*x*)KNNS-*x*BNKZSH ceramics with *x*=0.01, the peak intensity of $(002)_{pc}$ (Figs. 2(b) and (d) show the ε_r-*T* curves of the ceramics. The addition of Sb^{5+}, $Bi_{0.5}Na_{0.5}ZrO_3$, or $Bi_{0.5}Na_{0.5}HfO_3$ increased the $T_{R\text{-}O}$ and decreased the $T_{O\text{-}T}$ of

(1-*x*)KNNS-*x*BNKZSH ceramics, in agreement with the results reported previously [11-13]. For the *x*=0.01 ceramics, the $T_{R\text{-}O}$ and $T_{O\text{-}T}$ values were identified as -60 ^{o}C and 100 ^{o}C, respectively, indicating the existence of a single O phase at room temperature. As *x* increased up to 0.02 and 0.03, $T_{R\text{-}O}$ rose to -54 ^{o}C and -40 ^{o}C, respectively, and $T_{O\text{-}T}$ dropped to 71 ^{o}C and 48 ^{o}C, respectively. For the ceramics with *x*=0.02, its $T_{R\text{-}O}$ value was more far away from room temperature than that of $T_{O\text{-}T}$ value. Furthermore, I_{200} of the ceramics with *x*=0.02 was obviously higher than I_{002}, suggesting the involvement of T phase [27]. Thus, it can be inferred that the ceramics with *x*=0.02 possessed an O-T phase at room temperature [27]. For the ceramics with *x*=0.03, its $T_{R\text{-}O}$ value was much lower than room temperature, while the $T_{O\text{-}T}$ value was slightly above room temperature, indicating an O-T phase coexistence at room temperature [27]. As *x* further increased up to 0.035, $T_{R\text{-}O}$ and $T_{O\text{-}T}$ overlapped with each other, leading to the formation of an R-T phase boundary at $T_{R\text{-}T}$ [23,25,26]. The $T_{R\text{-}T}$ of the ceramics with *x*=0.035 and 0.04 was very near room temperature at 31±20 ^{o}C and 5±5 ^{o}C, respectively, suggesting the coexistence of the R and T phases at the room temperature [23,25,26]. For the ceramics with *x*=0.05, its $T_{R\text{-}T}$ of -4 ^{o}C was much lower than room temperature. Therefore, only a single T phase should be seen in the ceramics with *x*=0.05 at room temperature. From the ε_r-*T* curves shown in Fig. 2(d), the values of $T_{R\text{-}T}$ were identified as 31±15 ^{o}C and 25±10 ^{o}C for M=Zr and Hf, respectively, in the 0.965KNNS-0.035BNKM ceramics. Since the $T_{R\text{-}T}$ values of these two compositions were very close to room temperature, both the R and T phases should coexist at room temperature. It is worth noting that the $T_{R\text{-}T}$ ranges of these two compositions were slightly narrower with respect to that of 0.965KNNS-0.035BNKZSH ceramics, indicating that Sn^{4+} substitution could also enhance the diffuse nature of phase transition of KNN-based ceramics [14-16]. However, no

anomalies were observed in the ε_r-T curves of 0.965KNNS-0.035BNKS ceramics [Fig. 2(d)], which further confirmed that 0.965KNNS-0.035BNKS ceramics exhibited a pseudocubic phase [23].

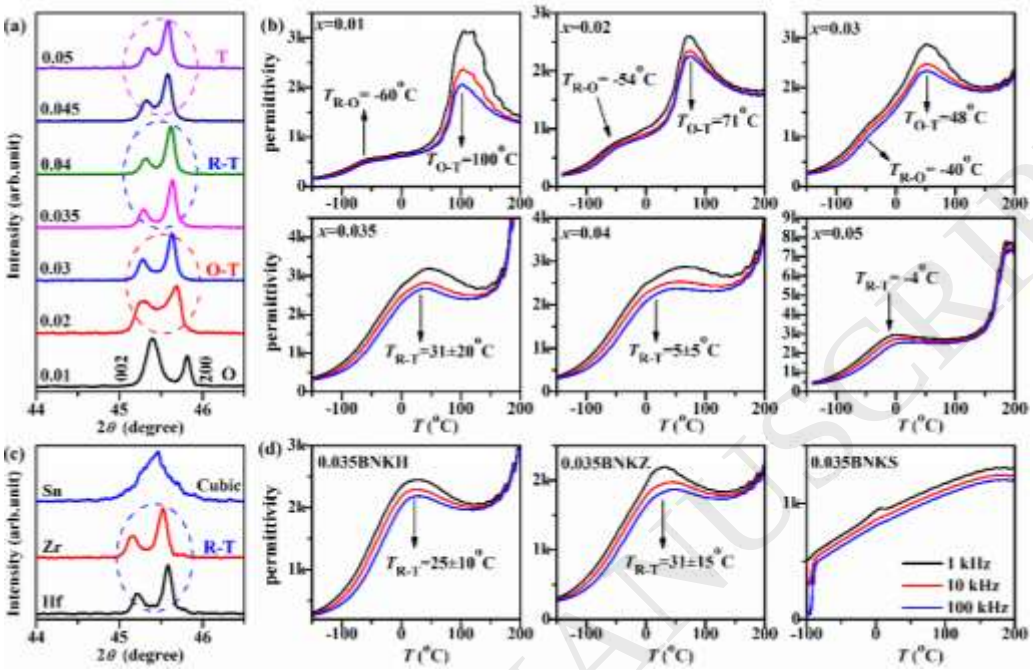

Figure 2. Enlarged XRD patterns of (a) (1-x)KNNS-xBNKZSH ceramics and (c) 0.965KNNS-0.035BNKM (M=Hf, Zr, and Sn) ceramics with 2θ=44-46°; and the ε_r-T (-150 °C-200 °C) curves of (b) (1-x)KNNS-xBNKZSH and (d) 0.965KNNS-0.035BNKM (M=Hf, Zr, and Sn) ceramics. The enlarged XRD patterns were indexed according to the pseudo-cubic phase structure axes.

Raman experiments, which are highly sensitive to changes in crystal structure, were performed to further analyze the phase transition [28]. Fig. 3(a) shows the temperature-dependent Raman spectra of 0.965KNNS-0.035BNKZSH ceramics. The vibrations of NbO_6 octahedra have six modes, $1A_{1g}(v_1)+1E_g(v_2)+2F_{1u}(v_3,v_4)+F_{2g}(v_5)+F_{2u}(v_6)$, where the stretching modes are $1A_{1g}(v_1)+1E_g(v_2)+1F_{1u}(v_3)$, and the rest are bending modes [28]. The v_1 mode, which represents a double degenerate symmetric O-Nb-O stretching vibration, is generally

employed to analyze phase transitions in KNN-based ceramics [29]. Here, the spectra within the range of 500-700 cm^{-1} were fitted to extract the shift of the v_1 mode using Lorentz fitting, as shown in the inset of Fig. 3(a) [29]. To clearly show the correlation between the structure and the properties of the ceramics, the Raman shift of the v_1 mode and the ε_r-T curve were plotted together in Fig. 3(b). As the temperature increased from -150 ^oC to 200 ^oC, the v_1 mode shifted to the lower wavenumber first, and then remained nearly unchanged, forming a plateau in the temperature range 0 $^oC \leq T \leq 75$ ^oC. As the temperature increased further, the v_1 mode shifted sharply to a lower wavenumber. This abrupt variation was also observed in KNN-LT ceramics [30]. Moreover, the R-T phase boundary observed in both the ε_r-T curve (T_{R-T}=31±20 ^oC) [Fig. 2(b)] and the Raman spectra (0 ^oC-75 ^oC) [Fig. 3(b)] was inferred to be a gradual phase transition (i.e., a diffused phase boundary) rather than an abrupt one [25]. Therefore, the experiments manifested that the addition of Sn^{4+} into KNN-based did construct the diffuse R-T phase boundary, further demonstrating the reliability of our design as mentioned above. Such a diffuse phase boundary highly suggested the possibility of good piezoelectricity and favorable temperature stability [17].

To further prove the existence of the R-T phase boundary, Rietveld refinements of 0.965KNNS-0.035BNKM {M=(Zr,Hf,Sn), Zr, and Hf} ceramics were also carried out. Fig. 3(c) shows the Rietveld refinement of 0.965KNNS-0.035BNKZSH ceramics. The Rietveld refinements of other two compositions were shown in Figures S5 (a-d) [see Supporting Information]. A good match between original data and fitting one was clearly observed, indicating the decent refinement process [Fig. 3(c)]. The detailed refinement results are listed in Table 1. Low values of R_w (<6.5%) and Sig (<1.6) further guaranteed the reliability of Rietveld refinements [31]. The space groups, $R3m$ and $P4mm$, respectively correspond to the R and T phases, demonstrating the

existence of R-T phase boundary. Moreover, an appreciable difference in the phase ratio was observed among these ceramics, which will be discussed to explain the difference of piezoelectricity among these compositions.

Previously, the flat Gibbs free energy could induce the easy polarization rotation, which accounted for the high piezoelectricity in lead-based piezoelectric ceramics with multiphase coexistence [32]. Here, the energy difference of the R-T phase boundary ($\Delta U_{R\text{-}T}$) was calculated using the $(K_{0.5}Na_{0.5})NbO_3$ mode with the lattice parameters listed in Table 1. The detailed energy value of each phase is listed in Table S2 [see Supporting Information]. The 0.965KNNS-0.035BNKM {M=(Zr,Hf,Sn), Zr, and Hf} ceramics possessed ultralow $\Delta U_{R\text{-}T}$ values of 2.9-5.5 meV. Previously, Cohen *et al*. calculated the energy difference between the R and T phases in $BaTiO_3$ as ΔU=6.42 meV [33]. Yao *et al*. reported an R-T phase coexistence in (1-*x*)KNNS-*x*BNKZ ($0.04 \leq x \leq 0.05$) thin films that exhibited an energy difference of $E_{T\text{-}R}$=0-0.02 eV [34]. The ultralow value of $\Delta U_{R\text{-}T}$ obtained in this work is comparable to these previous results, indicating a stable coexistence of the R and T phases. All of our results, from the XRD patterns, ε_r-*T* curves, temperature-dependent Raman spectra, and Rietveld refinement, confirmed the existence of an R-T phase boundary.

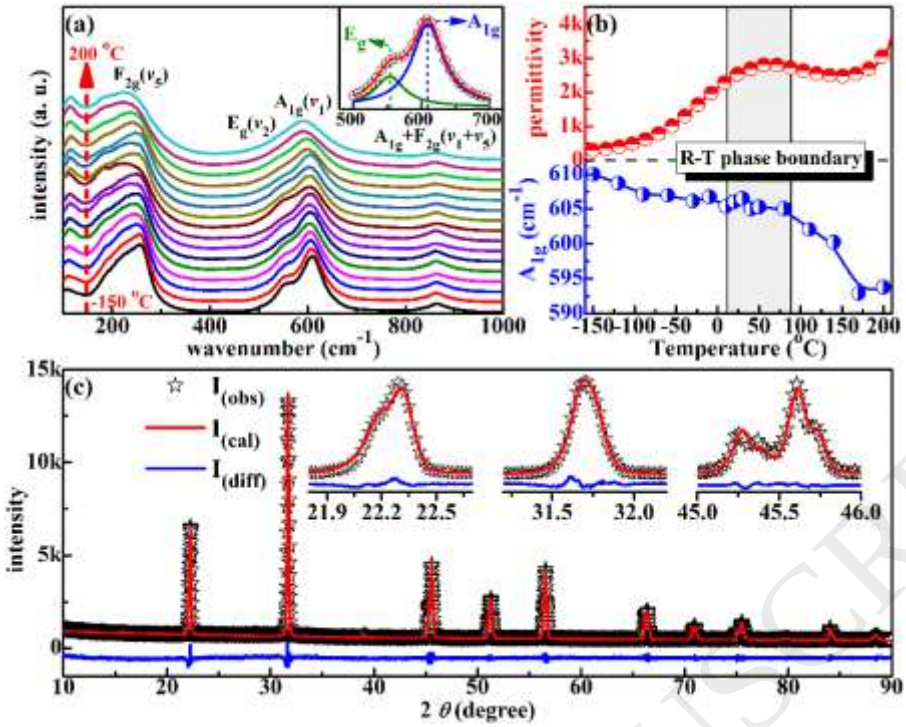

Figure 3. (a) Temperature-dependent Raman spectra of 0.965KNNS-0.035BNKZSH ceramics at different temperatures and fitting of Raman spectrum at T=-150 °C in the wavenumber range of 500-700 cm^{-1}. (b) Raman shift of A_{1g} (v_1) mode and permittivity of 0.965KNNS-0.035BNKZSH ceramics as a function of temperature. (c) Rietveld refinement of 0.965KNNS-0.035BNKZSH ceramics.

Figs. 4(a-g) and 4(h-j) show the ε_r-T curves of (1-x)KNNS-xBNKZSH and 0.965KNNS-0.035BNKM {M=Hf, Zr, and Sn} ceramics, respectively. Previous results showed that the addition of Sb^{5+}, $Bi_{0.5}Na_{0.5}ZrO_3$, or $Bi_{0.5}Na_{0.5}HfO_3$ decreased the T_c of KNN-based ceramics [11-13]. Although the T_c of the ceramics in this work also gradually reduced as the BNKZSH content increased, T_c was still about 240 °C at x=0.035. The T_c of 0.965KNNS-0.035BNKM {M=(Hf,Zr,Sn), Zr, Hf, and Sn} ceramics was indeed governed by the doping elements [Figs. 4(d) and (h-j)], i.e., 0.965KNNS-0.035BNKM {M=(Hf,Zr,Sn), Zr, and Hf} ceramics have a relatively high T_c in the range of 240-247 °C, while 0.965KNNS-0.035BNKS ceramics

exhibited a lower T_c of 200 ^oC. In addition to a lower T_c, 0.965KNNS-0.035BNKS ceramics also show a much broader and lower peak in the dielectric permittivity [Fig. 4(j)], which might be ascribed to the occurrence of ultra-fine grains [Fig. 1(g)] [35]. It was reported that the decreasing grain size could induce a weak dielectric relaxation and reduce dielectric permittivity [35]. Based on the values of T_{R-O}, T_{O-T}, T_{R-T}, and T_c from Fig. 2(b) and Figs. 4(a-g), a phase diagram was established for (1-*x*)KNNS-*x*BNKZSH ceramics, shown in Fig. 4(k). With increasing *x*, both T_c and T_{O-T} decreased, but T_{R-O} increased. Consequently, T_{O-T} and T_{R-O} converged, resulting in a direct phase transition between the R phase and the T phase at T_{R-T}. Since the T_{R-T} of the ceramics with *x*=0.035 and 0.04 was very close to room temperature, the R and T phases coexist at room temperature. A single T phase was observed in the ceramics with *x*=0.05 at room temperature because the T_{R-T} for these two compositions was much lower. The T_{R-T} and T_c values for 0.965KNNS-0.035BNKM {M=(Zr,Hf,Sn), Zr, Hf, and Sn} ceramics are also summarized in Fig. 4(l) for comparison. 0.965KNNS-0.035BNKM {M=(Zr,Hf,Sn), Zr and Hf} ceramics possessed the similar T_c values of 240-247 ^oC, while a low T_c value of 200 ^oC was found in 0.965KNNS-0.035BNKS ceramics.

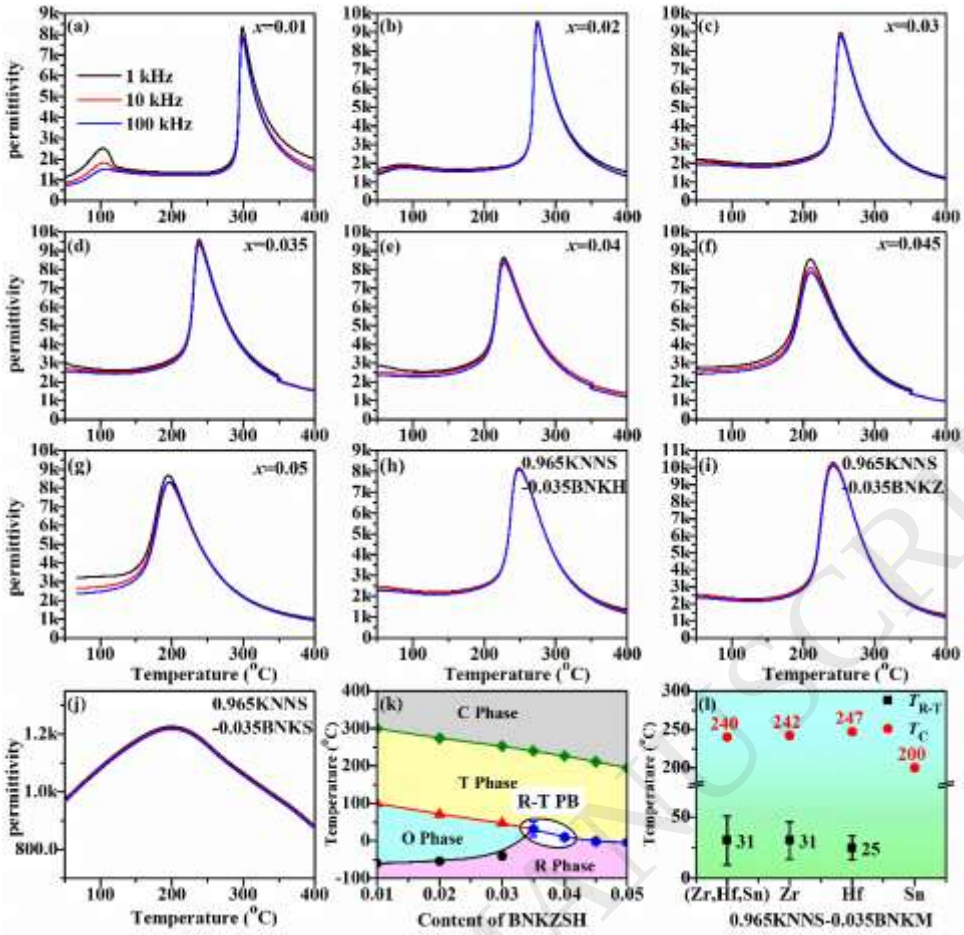

Figure 4. ε_r-T (50 °C-400 °C) curves of (a-g) (1-x)KNNS-xBNKZSH and (h-j) 0.965KNNS-0.035BNKM {M=(Zr,Hf,Sn), Zr, Hf, and Sn} ceramics. (k) Phase diagram of KNNS-xBNKZSH ceramics. (l) T_{R-T} and T_c of 0.965KNNS-0.035BNKM {M=(Zr,Hf,Sn), Zr, Hf, and Sn} ceramics.

Figs. 5(a) and (b) show the P-E hysteresis loops of (1-x)KNNS-xBNKZSH and 0.965KNNS-0.035BNKM {M=(Zr,Hf,Sn), Zr, Hf, and Sn} ceramics. As shown in Fig. 5(a), all of the samples showed a typical ferroelectric hysteresis loop. The saturation of P-E loops gradually reduced as x increased, suggesting that the addition of BNKZSH deteriorated the ferroelectricity of the KNN-based ceramics to some extent. Both the remanent polarization (P_r) and the coercive field (E_c) gradually decreased with an increase in x [Fig. 5(c)]. Saturated P-E loops were observed in the 0.965KNNS-0.035BNKM {M=(Zr,Hf,Sn), Zr, and Hf} ceramics that possessed an R-

T phase boundary [Fig. 5(b)]. However, an almost linear *P*-*E* loop was observed in 0.965KNNS-0.035BNKS ceramics [Fig. 5(b)], which was due to the high symmetry of the pseudocubic phase [Fig. 2(c)] and ultra-grain size [Fig. 1(g)] [35].

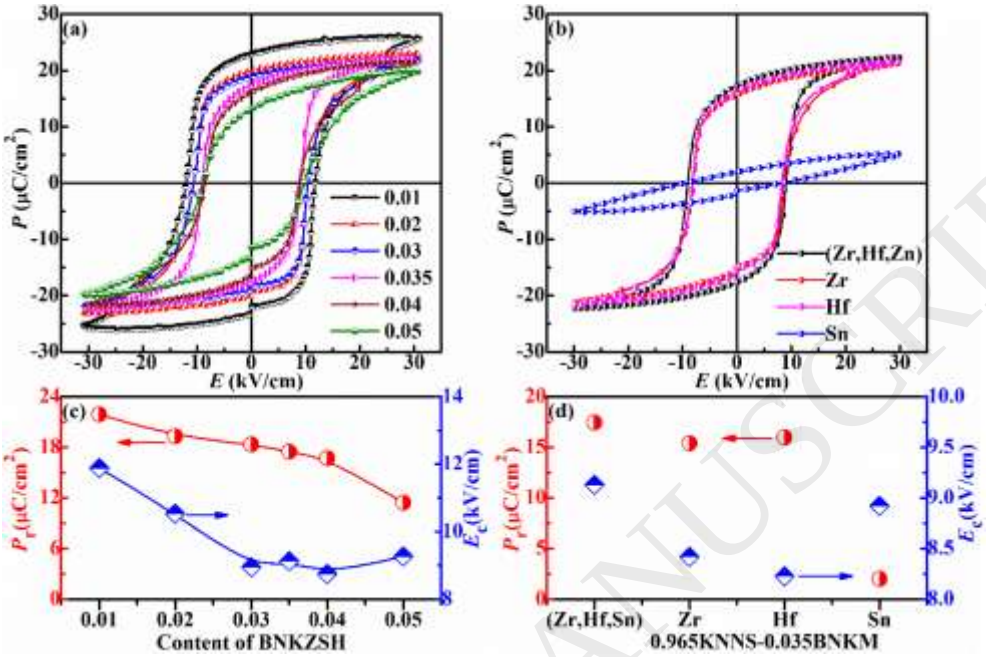

Figure 5. Polarization *vs.* electric field (*P*-*E*) loops of (a) KNNS-*x*BNKZSH and (b) KNNS-0.035BNKM {M=(Zr,Hf,Sn), Zr, Hf, and Sn} ceramics. Remanent polarization (P_r) and coercive field (E_c) of (c) KNNS-*x*BNKZSH and (d) KNNS-0.035BNKM {M=(Zr,Hf,Sn), Zr, Hf, and Sn} ceramics.

Figs. 6(a) and (b) show the dependence of ε_r and tan δ on *x* and M in (1-*x*)KNNS-*x*BNKZSH and 0.965KNNS-0.035BNKM {M=(Zr,Hf,Sn), Zr, Hf, and Sn} ceramics, respectively. In (1-*x*)KNNS-*x*BNKZSH ceramics, with increasing *x*, ε_r first increased and then decreased, leading to a maximum of 2700 at *x*=0.035 due to the R-T phase boundary [22-26], whereas tan δ (~0.045) remained nearly unchanged. In 0.965KNNS-0.035BNKM {M=(Zr,Hf,Sn), Zr, Hf, and Sn} ceramics, the values of ε_r depended on the additives, e.g., ε_r=2700, 2000, 2100, and 900 for the 0.965KNNS-0.035BNKM ceramics with M=(Zr,Hf,Sn), Zr, Hf, and Sn, respectively. Here, the R-

T phase boundary was mainly responsible for the enhanced ε_r in the 0.965KNNS-0.035BNKM {M=(Zr,Hf,Sn), Zr, and Hf} ceramics, while the degraded dielectric properties of 0.965KNNS-0.035BNKS ceramics were mainly caused by the occurrence of ultra-fine grains [Fig. 1(g)] [35]. The composition design (doping with different elements) clearly played an important role in the dielectric properties of the ceramics. Figs. 6(c) and (d) display the variation of d_{33} and k_p in (1-*x*)KNNS-*x*BNKZSH and 0.965KNNS-0.035BNKM {M=(Zr,Hf,Sn), Zr, Hf, and Sn} ceramics, respectively. With increasing *x*, d_{33} first increased and then decreased, leading to a maximum of d_{33}~465 pC/N at x=0.035; k_p was nearly independent of x when x<0.035, and then decreased when x>0.035 [Fig. 6(c)]. A comparison of d_{33} and k_p in 0.965KNNS-0.035BNKM {M=(Zr,Hf,Sn), Zr, Hf, and Sn) ceramics with different additives is shown in Fig. 6(d). All of the ceramics exhibited a large d_{33} (e.g., 410-465 pC/N) and a high k_p (e.g., 0.45-0.47), except 0.965KNNS-0.035BNKS ceramics, in which the piezoelectric properties could not be observed due to its pseudocubic phase structure [Fig. 2(c)]. It is widely recognized that both the phase structure and the domain structure are responsible for the piezoelectric properties of piezoelectric ceramics [36]. Generally, the multi-phase coexistence possesses the more possible polarization vectors than that of single phase, which could promote the polarization rotation and then benefit the piezoelectric properties [36]. Furthermore, due to the R-T phase boundary and the ultralow $\Delta U_{R\text{-}T}$ values in this work, a low polarization anisotropy was anticipated, which greatly promoted the polarization rotation and benefited the macroscopic piezoelectric properties [36]. As a result, 0.965KNNS-0.035BNKM {M=(Zr,Hf,Sn), Zr, and Hf) ceramics exhibited higher d_{33} values (e.g., 410-465 pC/N) than the other compositions due to the R-T phase boundary.

Furthermore, the observed difference of d_{33} values in 0.965KNNS-0.035BNKM {M=(Zr,Hf,Sn), Zr, and Hf} ceramics could be attributed to the T phase fraction and tetragonality (c/a). It was reported that that the piezoelectric properties of the piezoceramics, which possessed an O-T or R-T phase coexistence, were highly dependent on the T phase fraction and tetragonality (c/a), owing to the close relationship between piezoelectricity and crystalline symmetry [37-39]. More specifically, the larger piezoelectricity could be obtained in the piezoceramics that exhibited the higher T phase fraction and the larger tetragonality (c/a) [37-39]. Here, a comparison between the T/R phase ratio ($\gamma=T_{\text{fraction}}/R_{\text{fraction}}$) and the tetragonality (c/a) of 0.965KNNS-0.035BNKM {M=(Zr,Hf,Sn), Zr, and Hf} ceramics (using the refinement results from Table 1) is shown in the inset of Fig. 6(d). Obviously, 0.965KNNS-0.035BNKZSH ceramics exhibited a higher γ and a larger tetragonality (c/a) than those of 0.965KNNS-0.035BNKM (M=Zr, Hf) ceramics, which accounted for the higher d_{33} value in 0.965KNNS-0.035BNKZSH ceramics.

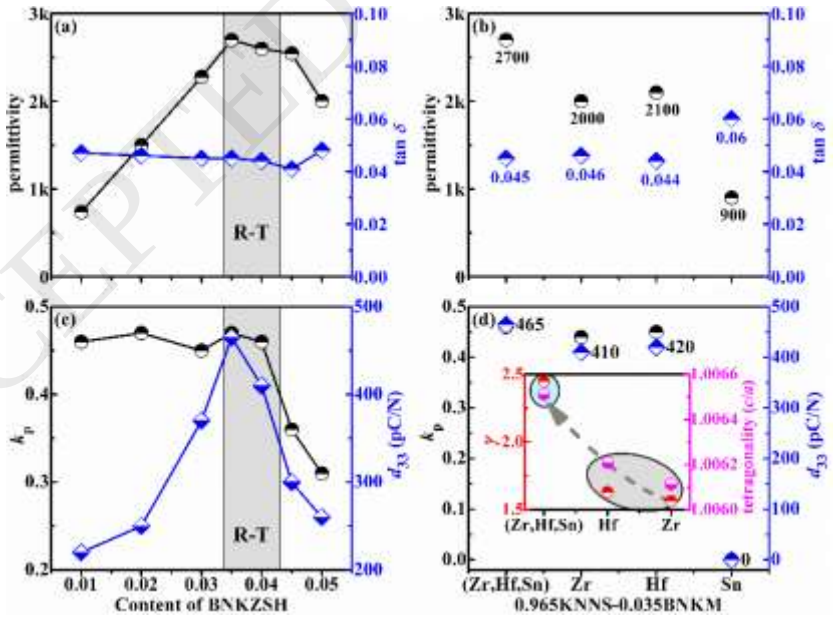

Figure 6. ε_r and tan δ of (a) (1-x)KNNS-xBNKZSH and (b) 0.965KNNS-0.035BNKM {M=(Zr,Hf,Sn), Zr, Hf, and Sn} ceramics. d_{33} and k_p of (c) (1-x)KNNS-

*x*BNKZSH and (d) 0.965KNNS-0.035BNKM {M=(Zr,Hf,Sn), Zr, Hf, and Sn} ceramics. The inset of (d) displays a comparison between the T/R phase ratio ($\gamma=T_{\text{fraction}}/R_{\text{fraction}}$) and tetragonality ($c/a$) of 0.965KNNS-0.035BNKM {M=(Zr,Hf,Sn), Zr, Hf, and Sn} ceramics.

Since domain structure plays a very critical role in determining the piezoelectricity of materials, vertical piezoresponse force microscopy (VPFM) was used to characterize the 0.965KNNS-0.035BNKZSH samples. The room-temperature piezoresponse and phase images are shown in the section of *in situ* temperature-dependent PFM analysis. Complicated domain structures caused by the coexistence of R and T phases, including striped and irregular domains, were observed at room temperature. Similar phenomena were also observed in the KNNS-BNKZ ceramics with an R-T phase boundary and account for the enhanced piezoelectric properties [40]. To gain a deeper understanding of the properties of the materials, the surface ferroelectric domains were written with a bias voltage of ±10 V, as shown schematically in Fig. 7(a). Fig. 7(b) displays the phase image, which was scanned immediately after writing. An appreciable contrast between the bright and dark areas was observed. The phase difference between the dark and bright areas was 175^{o} [Fig. 7(e)], indicating an ideal writing process and easy domain switching. The voltage required to completely switch the surface domains was about 10 V. Such a low driven-voltage was also observed in MnO_2-modified $(Na_{0.5}K_{0.5})NbO_3$-$(Bi_{0.5}Li_{0.5})TiO_3$-$BaZrO_3$ ceramics with an R-T phase boundary [41]. Figs. 7(c) and (d) show the phase images after writing for 30 and 60 minutes, respectively. The phase contrast faded slightly, indicating relaxation of ferroelectric domains. The corresponding phase histograms also reflected the relaxation, accompanied by a reduced phase difference of 163.5^{o} [Fig. 7(e)]. However, the slight relaxation suggested a good aging resistance because the

piezoelectricity was closely related to the status of the domains, in terms of quantity and size [42]. Furthermore, the good aging resistance behavior was also experimentally supported by the ultralow $\Delta d_{33}/d_{33\text{initial}}$ value of 3.3% after aging 21 weeks [see Figure S6 in Supporting Information]. Therefore, the easy switching and slow relaxation of the domains also played an important role in the enhanced piezoelectricity in this work.

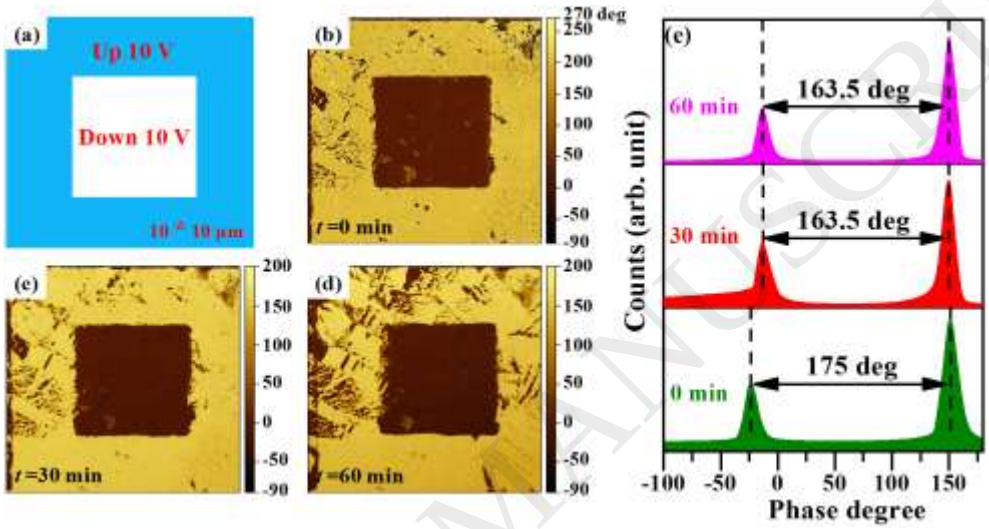

Figure 7. Vertical piezoresponse force microscopy (VPFM) of 0.965KNNS-0.035BNKZSH ceramics. (a) Sketch of driven electric field; Vertical phase images after writing for (b) 0 min, (c) 30 min, and (d) 60 min; (e) Phase histograms extracted from the VPFM phase images.

Fig. 8(a) displays the unipolar strain curves of 0.965KNNS-0.035BNKZSH ceramics, measured at E=20 kV/cm and 40 kV/cm. Converse piezoelectric coefficient d_{33}^* ($d_{33}^*=S_{max}/E_{max}$) values of 519 and 385 pm/V were respectively obtained at E=20 kV/cm and 40 kV/cm in 0.965KNNS-0.035BNKZSH ceramics, which were comparable to those of other representative KNN-based lead-free piezoceramics, as shown in Fig. 8(b) [5,10,17,23,40,41]. Fig. 8(c) shows the temperature-dependent unipolar strain curves of 0.965KNNS-0.035BNKZSH ceramics at E=40 kV/cm. As

the temperature increased from 25 °C to 80 °C, the maximum unipolar strain (S_{max} or S_{uni}) increased slightly. Then, S_{uni} gradually decreased at $T \geq 100$ °C, resulting in a $S_{uni(T)}/S_{uni(RT)}$ value of 1.0 and 0.74 at T=100 °C and 180 °C, respectively [Fig. 8(d)]. The temperature stability of the materials tested here is compared with several representative lead-free piezoceramics systems in Fig. 8(d) [5,10,23,41,43]. In this work, an almost constant $S_{uni(T)}/S_{uni(RT)}$ value of 1.0 was observed across a wide temperature range of 25-100 °C in the 0.965KNNS-0.035BNKZSH ceramics, which was comparable to those of KNN-BLT-BZ-Mn and KNNS-BNKH ceramics that exhibited the pronounced temperature stability and piezoelectricity [23,41]. The d_{33} and T_c of our materials, as well as those of several representative lead-free piezoelectric materials and soft PZT-4 ceramics [5-7,24,41,44-46], are presented for comparison in Table 2. Large d_{33} values ranging from 400 pC/N to 570 pC/N were recently obtained in KNN-based ceramics; however, the T_c was relatively low (e.g., 190-227 °C). Here, by adequately tuning the R-T phase boundary and composition of 0.965KNNS-0.035BNKZSH ceramics, a high d_{33} (~465 pC/N) and a high T_c (~240 °C) were simultaneously achieved. The d_{33} and T_c presented here were superior to those of BT- and BNT-based ceramics, and comparable to those of PZT4-based ceramics [see Table 2]. More importantly, a superior temperature stability was observed at 25 °C≤T≤100 °C.

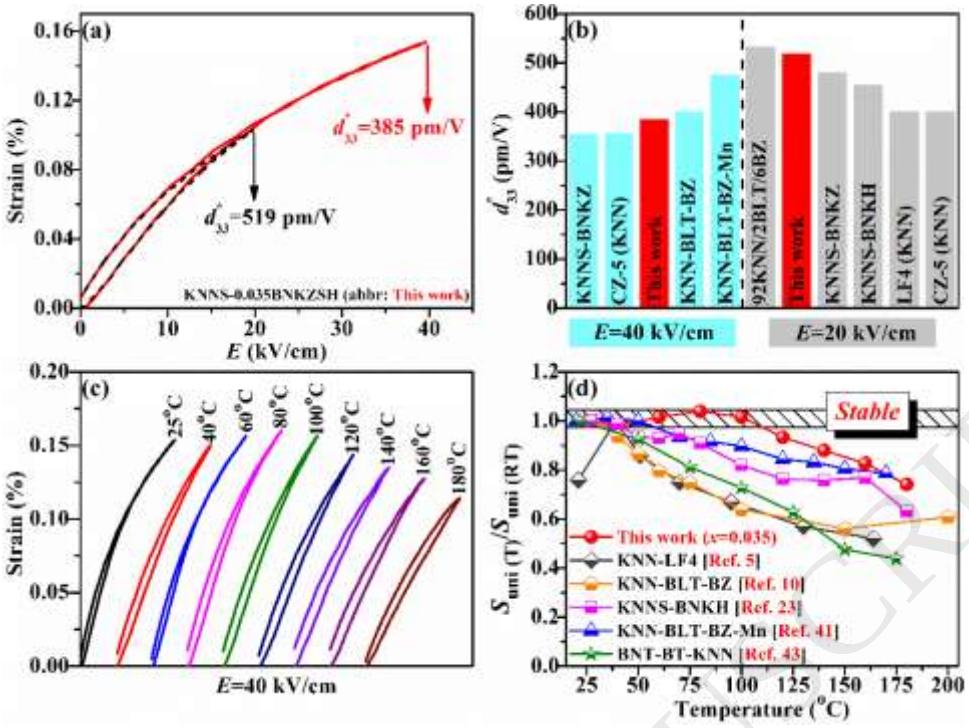

Figure 8. (a) Unipolar strain curves of 0.965KNNS-0.035BNKZSH ceramics at *E*=20 kV/cm and 40 kV/cm. (b) Comparison of d_{33}^* (S_{max}/E_{max}) among KNNS-0.035BNKZSH and other representative KNN-based lead-free piezoceramics at *E*=20 kV/cm and 40 kV/cm. (c) Temperature-dependent unipolar strain curves of 0.965KNNS-0.035BNKZSH ceramics at *E*=40 kV/cm. (d) Comparison of $S_{uni(T)}/S_{uni(RT)}$ among KNNS-0.035BNKZSH and other representative lead-free piezoceramic systems.

Here, *in situ* temperature-dependent VPFM measurements were performed to illuminate the physical mechanism behind the enhanced temperature stability. Both the vertical piezoresponse and the phase images were recorded as the temperature increased from 30 °C to 180 °C, as shown in Figs. 9(a-g). A representative area from the PFM images, marked by the white box, was inspected for variations. Within that representative area, both the brightness and sizes of ferroelectric domains were enhanced as the temperatures increased from 30 °C to 60 °C, as shown in the piezoresponse and phase images [Figs. 9(a) and (b) and Figs. 9(f) and (g)], indicating

the improved activity of the domains (e.g., domain switching and domain wall motion) [41,42,47]. Here, the improved activity of the domains was due to the increased thermal energy and diffuse R-T phase boundary in the 0.965KNNS-0.035BNKZSH ceramics, which possessed a broad R-T phase transition temperature of $T_{R\text{-}T}$=31±20 ºC [Fig. 2(b)]. Thus, a slight increase in temperature did not substantially affect the phase structure, but did enhance the activity of the domains (e.g., domain switching and domain wall motion). The enhanced activity of the domains also contributed to a slight increase in the unipolar strain at 25 ºC≤T≤80 ºC [Fig. 8(c)] [41,42,47]. When the temperature reached 100 ºC, both the piezoresponse and phase images were very similar to those at T=30 ºC, indicating a similar activity of the domains. Thus, the S_T/S_{RT} value of 1.0 was observed at T=100 ºC. As temperature increased further, both the brightness and the area of the domains gradually faded in both the piezoresponse and phase images, indicating the reduced domain structure in terms of response and quantity [41,42,47]. Here, the reduced domain structure at T≥100 ºC originated from the phase transition from R-T phase coexistence to a dominant (or even pure) tetragonal (T) phase and further increasing temperature. Generally, when a piezoelectric undergoes the phase transition from multiphase to a single phase, the domain configurations will inevitably reduce and be simplified owing to the complicated domain structure in multiphase coexistence [36,41,42,47]. Moreover, the further increasing temperature (T≥100 ºC) will gradually break the long-range order of ferroelectric domain structure [36,41,42,47]. Thus, both two factors are responsible for the reduced domain structure above 100 ºC. In spite of the reduced domain structure, a number of domains were still observed in both the piezoresponse and phase images at T=180 ºC [Figs. 9(e) and (g)], which accounted for the S_T/S_{RT} value of 0.74 at T=180 ºC [Fig. 8(c)]. In this way, the temperature stability

in 0.965KNNS-0.035BNKZSH ceramics (S_T/S_{RT} value of 1.0 at T=100 ºC) was enhanced by the stable domain structure.

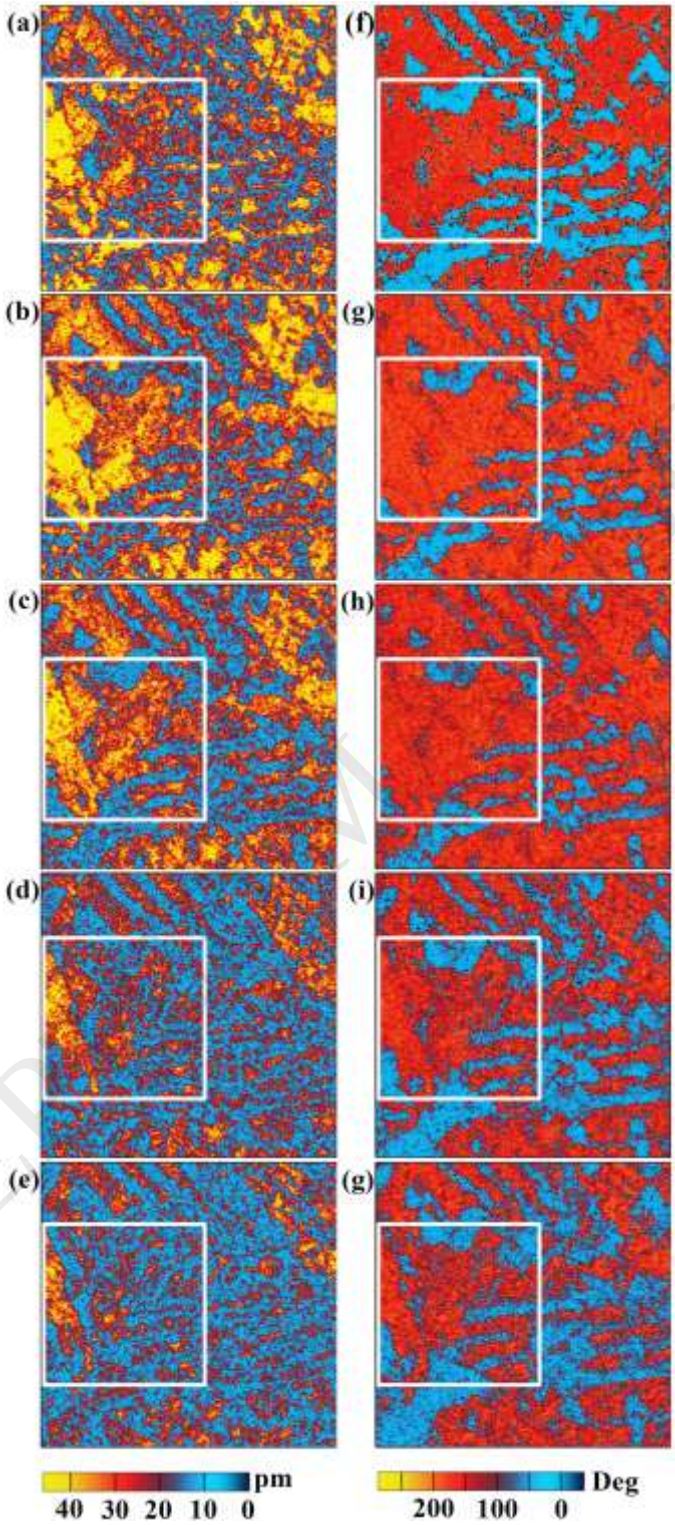

Figure 9. Vertical piezoresponse images of 0.965KNNS-0.035BNKZSH ceramics at (a) 30 ºC, (b) 60 ºC, (c) 100 ºC, (d) 140 ºC, and (e) 180 ºC. Corresponding vertical

phase images at (f) 30 ºC, (g) 60 ºC, (h) 100 ºC, (i) 140 ºC, and (g) 180 ºC. The measured area (white box) is 5μm×5μm.

4. Conclusion

In this work, (1-*x*)KNNS-*x*BNKZSH and 0.965KNNS-0.035BNKM (M=Zr, Hf, and Sn) ceramics were synthesized using the conventional solid-state reaction method. The effects of the additive BNKZSH on the microstructure, phase structure, and electrical properties of (1-*x*)KNNS-*x*BNKZSH ceramics were systematically investigated. Co-doping with Sb^{5+} and BNKZSH decreased $T_{O\text{-}T}$ and increased $T_{R\text{-}O}$, forming an R-T phase boundary in the ceramics with $0.035 \leq x \leq 0.04$. Due to the slight diffuse R-T phase boundary, the ceramics with x=0.035 showed enhanced electrical properties, accompanied by a large piezoelectricity (e.g., d_{33}~465 pC/N, k_p=0.47), a relatively high T_c of 240 ºC, and a superior temperature stability (i.e., unipolar strain remained almost unchanged at T=25-100 ºC). The enhanced electrical properties can mainly be attributed to the easy domain switching, high T phase ratio, and tetragonality (c/a) in the R-T phase boundary. The superior temperature stability was mainly due to the stable domain structures. Therefore, the construction of an R-T phase boundary and appropriate composition design substantially improved the piezoelectric properties and temperature stability. Thus, this work promotes the understanding of the performance and design of KNN-based lead-free ceramics.

Acknowledgements

This work is finished with the supporting of the National Natural Science Foundation of China (NSFC Nos. 51722208 and 51332003), the Key Technologies Research and Development Program of Sichuan Province (No. 2018JY0007) and the Graduate

Student's Research and Innovation Fund of Sichuan University (Nos. 2012017yjsy111, 2018YJSY009 and 2018YJSY071). The authors thank Mrs. Hui Wang (*Analytical & Testing Center of Sichuan University*) for measuring the FE-SEM images.

References

[1] T. Zheng, J. Wu, D. Xiao, J. Zhu, Recent Development in Lead-Free Perovskite Piezoelectric Bulk Materials. Prog. Mater. Sci. 98 (2018) 552-624.

[2] C.H. Hong, H.P. Kim, B.Y. Choi, H.S. Han, J.S. Son, C.W. Ahn, W. Jo, Lead-free piezoceramics-Where to move on? J. Materiomics. 2 (2016) 1-24.

[3] J.F. Li, K. Wang, F.Y. Zhu, L.Q. Cheng, F.Z. Yao, (K,Na)NbO_3-Based Lead Free Piezoceramics: Fundamental Aspects, Processing Technologies, and Remaining Challenges. J. Am. Ceram. Soc. 12 (2013) 3677-3696.

[4] J. Wu, D.Q. Xiao, J.G. Zhu, Potassium-Sodium Niobate Lead-Free Piezoelectric Materials: Past, Present, and Future of Phase Boundaries. Chem. Rev. 115 (2015) 2559-2595.

[5] Y. Saito, H. Takao, T. Tani, T. Nonoyama, K. Takatori, T. Homma, T. Nagaya, M. Nakamura, Lead-free piezoceramics. Nature 432 (2004) 84-87.

[6] X. Wang, J. Wu, D. Xiao, J. Zhu, X. Cheng, T. Zheng, B. Zhang, Giant piezoelectricity in potassium-sodium niobate lead-free ceramics. J. Am. Chem. Soc. 136 (2014) 2905-2910.

[7] K. Xu, J. Li, X. Lv, J. Wu, X. Zhang, D. Xiao, J. Zhu, Superior Piezoelectric Properties in Potassium-Sodium Niobate Lead-Free Ceramics. Adv. Mater. 28 (2016) 8519-8523.

[8] T. Zheng, H. Wu, Y. Yuan, X. Lv, Q. Li, T. Men, C. Zhao, D. Xiao, J. Wu, K. Wang, The structural origin of enhanced piezoelectric performance and stability in lead free ceramics. Energy. Environ. Sci. 10 (2017) 528-537.

[9] J.S. Zhou, K. Wang, F.Z. Yao, T. Zheng, J. Wu, D. Xiao, J. Zhu, J.F. Li, Multi-scale thermal stability of niobate-based lead-free piezoceramics with large piezoelectricity. J. Mater. Chem. C 3 (2015) 8780-8787.

[10] R. Wang, K. Wang, F. Yao, J.F. Li, F.H. Schader, K.G. Webber, W. Jo, J. Rödel, Temperature stability of lead-free niobate piezoceramics with engineered morphotropic phase boundary. J. Am. Ceram. Soc. 98 (2015) 2177-2182.

[11] R. Zuo, J. Fu, D. Lv, Y. Liu, Antimony Tuned Rhombohedral-Orthorhombic Phase Transition and Enhanced Piezoelectric Properties in Sodium Potassium Niobate. J. Am. Ceram. Soc. 93 (2010) 2783-2787.

[12] D. Wang, F. Hussain, A. Khesro, A. Feteira, Y. Tian, Q. Zhao, I.M. Reaney, Composition and temperature dependence of structure and piezoelectricity in (1-x)($K_{1-y}Na_y$)NbO_3-x($Bi_{1/2}Na_{1/2}$)ZrO_3 lead-free ceramics. J. Am. Ceram. Soc. 100 (2017) 627-637.

[13] H. Tao, J. Wu, T. Zheng, X. Wang, X. Lou, New (1-x)$K_{0.45}Na_{0.55}Nb_{0.96}Sb_{0.04}O_3$-$x$$Bi_{0.5}Na_{0.5}HfO_3$ lead-free ceramics: Phase boundary and their electrical properties. J. Appl. Phys. 118 (2015) 044102.

[14] W. Janbua, T. Bongkarn, T. Kolodiazhnyi, N. Vittayakorn, High piezoelectric response and polymorphic phase region in the lead-free piezoelectric $BaTiO_3$-$CaTiO_3$-$BaSnO_3$ ternary system. RSC Adv. 7 (2017) 30166-30176.

[15] L.F. Zhu, B.P. Zhang, X.K. Zhao, L. Zhao, F.Z. Yao, X. Han, P.F. Zhou, J.F. Li, Phase transition and high piezoelectricity in $(Ba,Ca)(Ti_{1-x}Sn_x)O_3$ lead-free ceramics. Appl. Phys. Lett. 103 (2013) 072905.

[16] Y. Yao, C. Zhou, D. Lv, D. Wang, H. Wu, Y. Yang, X. Ren, Large piezoelectricity and dielectric permittivity in $BaTiO_3$-$x$$BaSnO_3$ system: The role of phase coexisting. EPL 98 (2012) 27008-27013.

[17] F.Z. Yao, K. Wang, W. Jo, K.G. Webber, T.P. Comyn, J.X. Ding, B. Xu, L.Q. Cheng, M.P. Zheng, Y.D. Hou, Diffused Phase Transition Boosts Thermal Stability of High-Performance Lead-Free Piezoelectrics. Adv. Funct. Mater. 26 (2016) 1217-1224.

[18] R.D. Shannon, Revised effective ionic radii and systematic studies of interatomic distances in halides and chalcogenides, Acta Cryst. A 32 (1976) 751.

[19] A. Hewat, Cubic-tetragonal-orthorhombic-rhombohedral ferroelectric transitions in perovskite potassium niobate: neutron powder profile refinement of the structures. J. Phys. C: Solid State Phys. 6 (1973) 2559.

[20] S.J. Clark, M.D. Segall, C.D. Pickard, P.J. Hasnip, M.I. Probert, K. Refson, M.C. Payne, First principles methods using CASTEP. Z. Krist. Cryst. Mater. 220 (2005) 567-570.

[21] L. Bellaiche, D. Vanderbilt, Virtual crystal approximation revisited: application to dielectric and piezoelectric properties of perovskites. Phys. Rev. B 61 (2000) 7877.

[22] J. Xing, Z. Tan, L. Jiang, Q. Chen, J. Wu, W. Zhang, D. Xiao, J. Zhu, Phase structure and piezoelectric properties of (1-x)$K_{0.48}Na_{0.52}Nb_{0.95}Sb_{0.05}O_3$-$x$($Bi_{0.5}Na_{0.5}$)$_{0.9}$($Li_{0.5}Ce_{0.5}$)$_{0.1}ZrO_3$ lead-free piezoelectric ceramics. J. Appl. Phys. 119 (2016) 034101.

[23] T. Zheng, J. Wu, D. Xiao, J. Zhu, X. Wang, L. Xin, X. Lou, Strong Piezoelectricity in (1-x)($K_{0.4}Na_{0.6}$)($Nb_{0.96}Sb_{0.04}$)O_3-$xBi_{0.5}K_{0.5}Zr_{1-y}Sn_yO_3$ Lead-Free Binary System: Identification and Role of Multiphase Coexistence. ACS Appl. Mater. Interfaces 7 (2015) 5927-5937.

[24] K. Wang, F.Z. Yao, W. Jo, D. Gobeljic, V.V. Shvartsman, D.C. Lupascu, J.F. Li, J. Rödel, Temperature-Insensitive (K,Na)NbO_3-Based Lead-Free Piezoactuator Ceramics. Adv. Funct. Mater. 23 (2013) 4079-4086.

[25] F. Rubio-Marcos, R. López-Juárez, R.E. Rojas-Hernandez, A. Del Campo, N. Razo-Pérez, J.F. Fernandez, Lead-Free Piezoceramics: Revealing the Role of the Rhombohedral-Tetragonal Phase Coexistence in Enhancement of the Piezoelectric Properties. ACS Appl. Mater. Interfaces 7 (2015) 23080-23088.

[26] X. Lv, Z. Li, J. Wu, J. Xi, M. Gong, D. Xiao, J. Zhu, Enhanced piezoelectric properties in potassium-sodium niobate-based ternary ceramics. Mater. Design. 109 (2016) 609-614.

[27] H. Yamada, T. Matsuoka, H. Kozuka, M. Yamazaki, K. Ohbayashi, T. Ida, Crystal structure and phase transition behavior in ($K_{1-x}Na_x$)NbO_3-based lead-free piezoelectric ceramic over a wide range of temperatures. J. Appl. Phys. 120 (2016) 214102.

[28] F. Rubio-Marcos, M. Banares, J. Romero, J. Fernandez, Correlation between the piezoelectric properties and the structure of lead-free KNN-modified ceramics, studied by Raman Spectroscopy. J. Raman. Spectrosc. 42 (2011) 639-643.

[29] F. Rubio-Marcos, J.J. Romero, D.A. Ochoa, J.E. García, R. Perez, J.F. Fernandez, Effects of Poling Process on KNN-Modified Piezoceramic Properties. J. Am. Ceram. Soc. 93 (2010) 318-321.

[30] Y. Dai, X. Zhang, G. Zhou, Phase transitional behavior in $K_{0.5}Na_{0.5}NbO_3$-$LiTaO_3$ ceramics. Appl. Phys. Lett. 90 (2007) 262903.

[31] B. Narayan, J.S. Malhotra, R. Pandey, K. Yaddanapudi, P. Nukala, B. Dkhil, A. Senyshyn, R. Ranjan, Electrostrain in excess of 1% in polycrystalline piezoelectrics. Nat. Mater. 17 (2018) 427-431.

[32] W. Cao, L.E. Cross, Theoretical model for the morphotropic phase boundary in lead zirconate-lead titanate solid solution. Phys. Rev. B 47 (1993) 4825.

[33] H. Fu, R.E. Cohen, Polarization rotation mechanism for ultrahigh electromechanical response in single-crystal piezoelectrics. Nature 403 (2000) 281-283.

[34] Y. Wang, K. Yao, X. Qin, M.S. Mirshekarloo, X. Liu, F.E.H. Tay, High Piezoelectric Performance and Phase Transition in Stressed Lead-Free (1-*x*)(K,Na)(Sb,Nb)O_3-*x*(Bi,Na,K)ZrO_3 Thin Films. Adv. Electron. Mater. 3 (2017) 1700033.

[35] J. Hao, W. Bai, W. Li, J. Zhai, Correlation Between the Microstructure and Electrical Properties in High-Performance $(Ba_{0.85}Ca_{0.15})(Zr_{0.1}Ti_{0.9})O_3$ Lead-Free Piezoelectric Ceramics. J. Am. Ceram. Soc. 95 (2012) 1998-2006.

[36] M. Acosta, N. Novak, V. Rojas, S. Patel, R. Vaish, J. Koruza, G. Rossetti Jr, J. Rödel, $BaTiO_3$-based piezoelectrics: Fundamentals, current status, and perspectives. Appl. Phys. Rev. 4 (2017) 041305.

[37] F. Rubio-Marcos, J. Romero, M. Navarro-Rojero, J. Fernandez, Effect of ZnO on the structure, microstructure and electrical properties of KNN-modified piezoceramics. J. Eur. Ceram. Soc. 29 (2009) 3045-3052.

[38] R. Nie, Q. Zhang, Y. Yue, H. Liu, Y. Chen, Q. Chen, J. Zhu, P. Yu, D. Xiao, Phase structure-electrical property relationships in $Pb(Ni_{1/3}Nb_{2/3})O_3$-$Pb(Zr,Ti)O_3$-based ceramics. J. Appl. Phys. 119 (2016) 124111.

[39] X. Lv, J. Wu, J. Zhu, D. Xiao, X. Zhang, A New Method to Improve the Electrical Properties of KNN-based Ceramics: Tailoring Phase Fraction. J. Eur. Ceram. Soc. 38 (2017) 85-94.

[40] Y. Qin, J. Zhang, W. Yao, C. Lu, S. Zhang, Domain Configuration and Thermal Stability of $(K_{0.48}Na_{0.52})(Nb_{0.96}Sb_{0.04})O_3$-$Bi_{0.50}(Na_{0.82}K_{0.18})_{0.50}ZrO_3$ Piezoceramics with High d_{33} Coefficient. ACS Appl. Mater. Interfaces 8 (2016) 7257-7265.

[41] M.H. Zhang, K. Wang, Y.J. Du, G. Dai, W. Sun, G. Li, D. Hu, H.C. Thong, C. Zhao, X.Q. Xi, High and temperature-insensitive piezoelectric strain in alkali niobate lead-free perovskite. J. Am. Chem. Soc. 139 (2017) 3889-3895.

[42] Q. Liu, F.Y. Zhu, L. Zhao, K. Wang, L. Li, J.F. Li, Further Enhancing Piezoelectric Properties by Adding MnO_2 in $AgSbO_3$-Modified $(Li,K,Na)(Nb,Ta)O_3$ Lead-Free Piezoceramics. J. Am. Ceram. Soc. 99 (2016) 3670-3676.

[43] S.T. Zhang, A.B. Kounga, E. Aulbach, W. Jo, T. Granzow, H. Ehrenberg, J. Rödel, Lead-free piezoceramics with giant strain in the system $Bi_{0.5}Na_{0.5}TiO_3$-

$BaTiO_3$-$K_{0.5}Na_{0.5}NbO_3$. II. Temperature dependent properties. J. Appl. Phys. 103 (2008) 034108-1.

[44] S.T. Zhang, A.B. Kounga, E. Aulbach, H. Ehrenberg, J. Rödel, Giant strain in lead-free piezoceramics $Bi_{0.5}Na_{0.5}TiO_3$-$BaTiO_3$-$K_{0.5}Na_{0.5}NbO_3$ system. Appl. Phys. Lett. 91 (2007) 112906.

[45] J. Zhang, Z. Pan, F.F. Guo, W.C. Liu, H. Ning, Y. Chen, M.H. Lu, B. Yang, J. Chen, S.T. Zhang, Semiconductor/relaxor 0-3 type composites without thermal depolarization in $Bi_{0.5}Na_{0.5}TiO_3$-based lead-free piezoceramics. Nat. Commun. 6 (2015) 6615.

[46] W. Liu, X. Ren, Large piezoelectric effect in Pb-free ceramics. Phys. Rev. Lett. 103 (2009) 257602.

[47] Y. Liu, Y. Chang, F. Li, B. Yang, Y. Sun, J. Wu, S. Zhang, R. Wang, W. Cao, Exceptionally High Piezoelectric Coefficient and Low Strain Hysteresis in Grain-Oriented (Ba,Ca)(Ti,Zr)O_3 through Integrating Crystallographic Texture and Domain Engineering. ACS Appl. Mater. Interfaces 9 (2017) 29863-29871.

Table 1. Rietveld refinement results for 0.965KNNS-0.035BNKM {M=(Zr,Hf,Sn), Zr, and Hf} ceramics.

Composition	Space group	Lattice parameter*			Phase ratio	R_w (%)	Sig	$\Delta U_{T\text{-}R}$ (meV)
		a=b (Å)	c (Å)	α (°)				
0.965KNNS	*R*3*m*	3.9823 (6)		89.97	0.29	6.05	1.53	5.5
	*P*4*mm*	3.9729 (1)	4.0028 (1)	90	0.71			

0.965KNNS-0.035BNKZSH	*R*3*m*	3.9815 (4)	89.98	0.39			
	*P*4*mm*	4.0013 (9)			5.65	1.49	4.4
		3.9770 (7)	90	0.61			
0.965KNNS-0.035BNKH	*R*3*m*	3.9788 (1)	89.95	0.38			
	*P*4*mm*	4.0015 (3)			6.16	1.57	2.9
		3.9768 (3)	90	0.62			

* Due to the intrinsic symmetry, $a=b=c$ for the *R*3*m* space group, and $a=b$ for the *P*4*mm* space group.

Table 2: Comparison among d_{33}, $T_{c,}$ and phase boundaries of several representative piezoelectric material systems.

Material system	d_{33} (pC/N)	T_C (°C)	Phase boundary	Reference
KNNS-BNKZSH	465	240	R-T	This work
Textured LF4T	416	253	O-T	5
KNNLT-CZ-MnO_2	300	200	O-T	24
KNNS-BNKZ	490	227	R-T	6
KNNS-BZ-BKH	570	190	R-T	7
KNN-BLT-BZ-MnO_2	340	243	R-T	41
BNT-BT-KNN	<100	T_d<200	—	44
BNT-BT: ZnO	<200	280	—	45
BZT-BCT	620	90	C-R-T	46
PZT4	410	250	R-T	5

Figure captions

Figure 1. FE-SEM images of polished and thermally etched cross-sections of KNNS-*x*BNKZSH ceramics with (a) *x*=0.01, (b) *x*=0.02, (c) *x*=0.035, (d) *x*=0.05, and 0.965KNNS-0.035BNKM ceramics with (e) M=Zr, (f) M=Hf and (g) M=Sn. (h) Average grain size (AGS) of the ceramics in this work.

Figure 2. Enlarged XRD patterns of (a) (1-*x*)KNNS-*x*BNKZSH ceramics and (c) 0.965KNNS-0.035BNKM (M=Hf, Zr, and Sn) ceramics with 2θ=44-46°; and the ε_r-*T* (-150 °C-200 °C) curves of (b) (1-*x*)KNNS-*x*BNKZSH and (d) 0.965KNNS-0.035BNKM (M=Hf, Zr, and Sn) ceramics. The enlarged XRD patterns were indexed according to the pseudo-cubic phase structure axes.

Figure 3. (a) Temperature-dependent Raman spectra of 0.965KNNS-0.035BNKZSH ceramics at different temperatures and fitting of Raman spectrum at T=-150 ^{o}C in the wavenumber range of 500-700 cm^{-1}. (b) Raman shift of A_{1g} (v_1) mode and permittivity of 0.965KNNS-0.035BNKZSH ceramics as a function of temperature. (c) Rietveld refinement of 0.965KNNS-0.035BNKZSH ceramics.

Figure 4. ε_r-T (50 ^{o}C-400 ^{o}C) curves of (a-g) (1-x)KNNS-xBNKZSH and (h-j) 0.965KNNS-0.035BNKM {M=(Zr,Hf,Sn), Zr, Hf, and Sn} ceramics. (k) Phase diagram of KNNS-xBNKZSH ceramics. (l) T_{R-T} and T_c of 0.965KNNS-0.035BNKM {M=(Zr,Hf,Sn), Zr, Hf, and Sn} ceramics.

Figure 5. Polarization *vs.* electric field (P-E) loops of (a) KNNS-xBNKZSH and (b) KNNS-0.035BNKM {M=(Zr,Hf,Sn), Zr, Hf, and Sn} ceramics. Remanent polarization (P_r) and coercive field (E_c) of (c) KNNS-xBNKZSH and (d) KNNS-0.035BNKM {M=(Zr,Hf,Sn), Zr, Hf, and Sn} ceramics.

Figure 6. ε_r and tan δ of (a) (1-x)KNNS-xBNKZSH and (b) 0.965KNNS-0.035BNKM {M=(Zr,Hf,Sn), Zr, Hf, and Sn} ceramics. d_{33} and k_p of (c) (1-x)KNNS-xBNKZSH and (d) 0.965KNNS-0.035BNKM {M=(Zr,Hf,Sn), Zr, Hf, and Sn} ceramics. The inset of (d) displays a comparison between the T/R phase ratio (γ=$T_{fraction}$/$R_{fraction}$) and tetragonality (c/a) of 0.965KNNS-0.035BNKM {M=(Zr,Hf,Sn), Zr, Hf, and Sn} ceramics.

Figure 7. Vertical piezoresponse force microscopy (VPFM) of 0.965KNNS-0.035BNKZSH ceramics. (a) Sketch of driven electric field; Vertical phase images after writing for (b) 0 min, (c) 30 min, and (d) 60 min; (e) Phase histograms extracted from the VPFM phase images.

Figure 8. (a) Unipolar strain curves of 0.965KNNS-0.035BNKZSH ceramics at E=20 kV/cm and 40 kV/cm. (b) Comparison of d_{33}^* (S_{max}/E_{max}) among KNNS-0.035BNKZSH and other representative KNN-based lead-free piezoceramics at E=20 kV/cm and 40 kV/cm. (c) Temperature-dependent unipolar strain curves of 0.965KNNS-0.035BNKZSH ceramics at E=40 kV/cm. (d) Comparison of $S_{uni(T)}/S_{uni(RT)}$ among KNNS-0.035BNKZSH and other representative lead-free piezoceramic systems.

Figure 9. Vertical piezoresponse images of 0.965KNNS-0.035BNKZSH ceramics at (a) 30 ºC, (b) 60 ºC, (c) 100 ºC, (d) 140 ºC, and (e) 180 ºC. Corresponding vertical phase images at (f) 30 ºC, (g) 60 ºC, (h) 100 ºC, (i) 140 ºC, and (g) 180 ºC. The measured area (white box) is 5μm×5μm.

Table 1. Rietveld refinement results for 0.965KNNS-0.035BNKM {M=(Zr,Hf,Sn), Zr, and Hf} ceramics.

Table 2: Comparison among d_{33}, T_c, and phase boundaries of several representative piezoelectric material systems.